

Investigation of Geometric RDC Dependencies Using a Fast Reactive Euler Solver

Roman Klopsch*, Niclas Garan†, Eric Bach‡, Christian Oliver Paschereit§ and Myles D. Bohon¶
Technische Universität Berlin, 10623 Berlin, Germany

A time resolved, two-dimensional reactive Euler solver is employed to simulate Rotating Detonation Combustion (RDC). The influence of combustor diameter, axial length, combustion annulus mass flux, outlet throat area, and air injector area on the flow field geometry and performance is studied. There is a similarity in the unsteady outlet state for cases at equal combustor aspect ratio. It is demonstrated that generalization of Equivalent Available Pressure methodology for the non-constant heat capacity ratio case is not trivial and can introduce significant errors. To bypass this issue, an alternative approach for performance quantification is introduced. Mass flux and outlet throat area are found to have a significantly stronger effect on performance compared to diameter and axial length. Yet, the influence of the latter two is significant. The angle of the oblique shock is quantified and is shown to correlate with the ratio of detonation height and axial combustor length. The results suggest that entropy generation due to shock processing is the driving mechanism behind performance deviation due to changes in combustor diameter and axial length. Approximate predictions about the shock processing can be made using geometric dependencies of the flow field.

Nomenclature

Symbols

A	= annulus cross-section area
D	= annulus diameter
H	= detonation height
h	= enthalpy
J	= mass flux
L	= combustor length
p	= pressure
q	= specific heat release
s	= entropy
T	= temperature
u	= velocity
v	= detonation wave speed
x	= circumferential combustor coordinate
z	= axial combustor coordinate
γ	= ratio of specific heats
ϕ	= equivalence ratio
ρ	= density
θ	= azimuthal angle
$(\cdot)_s$	= static
$(\cdot)_t$	= total (lab. frame)

Acronyms

EAP	= Equivalent Available Pressure
IAW	= Isentropically Available Work
pd	= Power Density (local)
PD	= Power Density (integral)
PDC	= Pulse Detonation Combustion
PG	= Pressure Gain
PGC	= Pressure Gain Combustion
RDC	= Rotating Detonation Combustion
RMSD	= Root-Mean-Square Deviation
SEC	= Shockless Explosion Combustion

Station Numbers

2	= air plenum
3.1	= air injector throat
3.2	= combustion annulus
8	= outlet throat
10	= end of exhaust expansion
f	= fuel plenum

*Undergraduate Student, Chair of Pressure Gain Combustion, TU Berlin, AIAA Student Member.

†PhD Student, Chair of Combustion Kinetics, TU Berlin.

‡Postdoctoral Researcher, Chair of Pressure Gain Combustion, TU Berlin, AIAA Student Member.

§Professor, Chair of Fluid Dynamics, TU Berlin, AIAA Associate Fellow

¶Professor, Chair of Pressure Gain Combustion, TU Berlin, AIAA Member.

I. Introduction

In recent decades, various efforts have been made to reduce the carbon impact of the energy and transportation sectors. Among other pathways, hydrogen is going to play an important role in this process. As a consequence, (hydrogen-ready) gas turbines have been given special attention. However, the thermal efficiency of conventional gas turbines is approaching thermodynamic limitations inherent to the Joule cycle. Further major improvements therefore become more and more difficult and increased attention has been given to the utilization of different thermodynamic cycles. By constraining the volume during the combustion process, entropy generation can be reduced and efficiency subsequently increased [1]. The limiting of expansion during heat addition leads to an increase in the fluid's stagnation pressure, hence Pressure Gain Combustion (PGC).

Several technologies have been developed to achieve PGC, with the most prominent being pulse detonation combustion (PDC), shockless explosion combustion (SEC), and rotating detonation combustion (RDC). In contrast to PDC and SEC, which rely on cyclic recharging, the combustion process in an RDC is continuous. The feasibility of RDC engines has been demonstrated experimentally [2–5] and the process has been subject to various experimental and numerical studies mainly focusing on the underlying physical processes and the influence of boundary conditions. Simplified two-dimensional models [6], reduced order models [7] or high-fidelity 3D models [8] have been used to analyze RDC.

Up until now, limited attention has been given to the systematic geometric dependencies of RDC in terms of performance over varying global parameters of combustor design. The flow field geometry significantly affects RDC loss mechanisms but is difficult to study experimentally. In the case of combustor diameter, for example, a new test article would have to be built for each investigated value while requiring laboratory infrastructure with a large controllable range. In numerical investigation, computational costs often prevent the investigation of large parameter spaces. Here, relatively fast analytical tools are needed to extend the understanding of RDC operation and performance. Yi et al. [9] studied the effect of wave number and axial length. Increasing either leads to an increase in total pressure loss and slightly improves propulsive performance. Tsuboi et al. [8] performed 2D and 3D numerical simulations and showed that the flow field structure and specific impulse (ISP) remain approximately unaffected by scale in the 2D case. In the 3D case, however, scale is found to be important due to curvature effects. RDE diameter and axial length have been varied individually in numerical simulations by Schwer and Kailasanath [10]. They found ISP to be unaffected by both when the exit is fully supersonic. For a partially subsonic exit, axial length is observed to effect ISP. There is, however, a loss mechanism expected to affect performance depending on diameter and axial length regardless of whether the exit is choked: irreversible processing occurs in the oblique shock and the fraction of the flow processed in the shock is determined by the flow field geometry.

In a previous work [11], we introduced a numerical model for the RDC based on the solution of the two-dimensional reactive Euler equations. The model is sufficiently simple to allow for relatively short turnaround times and thus analysis of a broad parameter space. The previous paper analyzed a parameter range covering different injector setups, mass flow rates and outlet restrictions. A similar parameter space was analyzed experimentally using the RDC rig at TU Berlin [2]. In the present paper, the main focus is on variations in the primary combustor design parameters, including: diameter, axial length, reactant mass flux, outlet restriction, and air injector area. The parameters' effect on the flow field and performance is quantified and related to the underlying loss mechanism.

II. Methods

The RDC model used for this study was described in detail in a previous study [11]. Therefore, only a brief overview is given here. The reactive Euler solver consists of an HLLE (Harten, Lax von Leer, Einfeldt) approximate Riemann solver using a second-order MUSCL-Hancock scheme for spatio-temporal reconstruction as well as a minmod flux limiter. A two-dimensional representation of the combustion annulus is derived by neglecting the radial dimension and thus "unrolling" the combustor into a rectangular domain with periodic boundary conditions at the left and right side. The inlet boundary is implemented as a reflecting wall, with source terms being applied to model the air and fuel injector individually. At the outlet boundary, the flow is isentropically expanded to ambient pressure (1 bar in this case). The momentum generated by this expansion is dropped, because the pressure can dissipate in all spatial dimensions. A two-step ignition delay mechanism with a heat release source term is used to save computational costs. The mechanism assumes two steps of combustion:

- 1) Buildup of radicals without any heat release (induction step).
- 2) Rapid recombination with instantaneous release of all reaction heat (recombination step).

The length of the induction step and the heat release source term are interpolated from tabulated values, which have

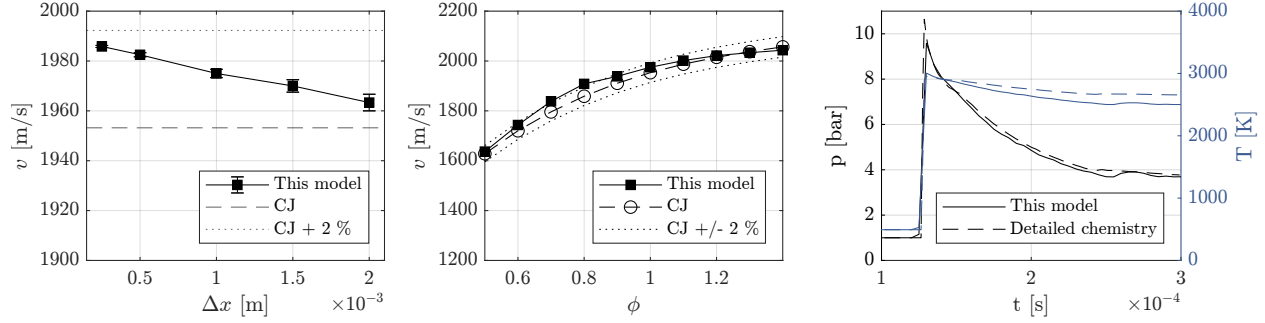


Fig. 1 Results of the 1D shock-tube validation: Predicted detonation wave speed at $\phi = 1$ for varying grid resolution (left) and varying equivalence ratio at $\Delta x = 1$ mm (mid) plotted against reference values. Pressure and Temperature traces for $\phi = 1$ and $\Delta x = 1$ mm plotted against results from detailed chemistry (right). Adapted from [11].

been determined in advance using a multi-step H_2 -Air mechanism [12] and the chemical kinetics solver Cantera [13]. A binary criterion based on pressure gradient is employed to differentiate between detonation and deflagration. For the latter, the heat release is distributed over multiple time-steps to approach isobaric heat release and prevent detonations from spawning in the absence of shock waves. The reader is referred to the previous paper for a more detailed description of the heat release mechanism.

We use the standard station designation as proposed by others [5, 14, 15] for this paper, with the air plenum as station no. 2, the air injector throat station no. 3.1, the combustion annulus in the detonation region as station no. 3.2, the exit throat as station no. 8, and the end of the exhaust stream expansion as station no. 10.

A. Numerical Validation

The combustion model has previously been validated [11] against a detailed chemistry mechanism [12] and the propagation speed of the detonation wave was compared with the corresponding CJ value obtained using the shock and detonation toolbox [16]. For this study, we extend the numerical validation with a mesh refinement study. The results are depicted in Figure 1. It can be seen that the wave speed deviates by less than 2% across the tested grid resolutions (left), that the close agreement with CJ-velocity holds for a wide range of equivalence ratios (middle), and that pressure and temperature traces also match results obtained using the detailed chemistry mechanism within acceptable range (right).

B. Solution Procedure

Due to the individual responses of the air- and fuel injectors to the flow field, defining the injection pressures to reach the desired flow conditions is difficult *a priori*. Instead, the injection pressures for both air and fuel are iteratively solved together with the flow field according to Equation 1 to generate solutions at the desired propellant mass flux and equivalence ratio. This means, that changes in the downstream conditions effect the injection pressures, while the injector flow rate remains approximately constant. The value for the constant slope in Eq. 1 is chosen in a trade-off between numerical stability/robustness and computation time. High values speed up the convergence process but might introduce oscillations and destabilize the scheme. In our case, a value of 0.1 kN s kg^{-1} for the air injector and 5 kN s kg^{-1} for the fuel injector leads to the model converging quickly and reliably towards the nominal values.

$$p_{\text{injec},n+1} = p_{\text{injec},n} + \text{const} \cdot (J_{\text{injec},\text{nominal}} - J_{\text{injec},\text{current}}) \quad (1)$$

A solution is considered converged when (i) the injection pressures for air and fuel are converged (i. e. the nominal flow rates are reached and have stabilized) and (ii) the mass flow rate at the outlet plane equals that at the inlet plane and remains approximately constant in time (i. e. stationary flow). All simulations are checked for anomalies and to assure they are quasi-stationary in their respective rotating frame.

Table 1 Parameters of the baseline case.

πD	L	$J_{3,2}$	$A_8/A_{3,2}$	$A_{3,1}/A_{3,2}$	$A_f/A_{3,2}$	ϕ	T_2	T_f
0.3 m	0.1 m	250 kg s ⁻¹ m ⁻²	0.8	0.15	0.01	1	300 K	300 K

Table 2 Range of varied parameters.

Parameter	Range	Unit
πD	(0.25, 0.3, ..., 0.5) and (0.6, 0.7, ..., 1)	m
L	(0.05, 0.075, ..., 0.2)	m
$J_{3,2}$	(100, 150, ..., 400)	kg s ⁻¹ m ⁻²
$A_8/A_{3,2}$	(0.4, 0.5, ..., 1)	-
$A_{3,1}/A_{3,2}$	(0.1, 0.125, ..., 0.3)	-

C. Parameter Space

To set up the parameter space, a representative baseline case is chosen. The parameters of the baseline case are defined according to Table 1. The effects of the parameters on the left of the double-line are studied, while the parameters on the right are held constant for all cases. Selected parameters are then varied individually to assess their effect in isolation. It should be noted that the studied parameters are not independent but are expected to display inter-dependencies. A different baseline case might therefore show significantly different sensitivity to each parameter. Consequently, parameter sensitivity should be interpreted qualitatively rather than quantitatively. The model used is not able to predict the operating mode of the RDC (e.g. the number of waves) but will instead converge towards a solution with the number of waves implied by the initial value. Assessment of the operating mode is beyond the scope of this work and therefore single wave operation is simulated for all cases. The respective range of each varied parameter is listed in Table 2.

III. Results

In total, 35 simulations are performed. In three cases, the solver did not converge to a stable solution ($J_{3,2} = 400 \text{ kg s}^{-1} \text{ m}^{-2}$, $A_8/A_{3,2} = 0.5$ and $A_8/A_{3,2} = 0.4$). It is unknown whether the failure of those cases is an artifact of the specific model applied in this work or represents an actual physical phenomenon. Those cases are excluded from the following analysis. For all other solutions, the converged mass flux and equivalence ratio match the respective nominal value within less than $\pm 1 \%$. To improve readability, not all figures display the full range of each parameter.

A. Unsteady Outlet State

The unsteady RDC outlet state is displayed in Figure 2 for varying combustor circumference (top row) and axial length (bottom row). Instantaneous temperature, static pressure, axial mass flux, and heat capacity ratio are plotted over the phase angle θ . The coordinate system is chosen so that the oblique shock is at $\theta = \pi$ and moving from left to right for all cases. It can be seen that both combustor circumference and axial length significantly impact the outlet state. The outlet state for small circumference and large axial length is generally smoother, and vice versa. This is a result of the greater distance between the detonation and the outlet: the detonation height (H) is approximately proportional to πD and approximately independent from L . The "wobble" seen closely behind the oblique shock is due to the slip line. With longer distances between the detonation and outlet plane, the azimuthal distance between the oblique shock and slip line increases and the slip line becomes less distinct. Interestingly, the outlet state (with respect to the phase angle θ) is quite similar for cases with similar combustor aspect ratio ($\pi D/L$). This is depicted in Figure 3. Here, the outlet state for cases with three different combustor aspect ratios are plotted. $\pi D/L = 3$ corresponds to the baseline case. The different aspect ratios have each been reached in two different ways: By varying πD while keeping L at the baseline value (solid lines) and by varying L while keeping πD at the baseline value (dashed lines). The values for $\pi D/L = 4$ are ($\pi D = 0.4 \text{ m}$, $L = 0.1 \text{ m}$) and ($\pi D = 0.3 \text{ m}$, $L = 0.075 \text{ m}$). The values for $\pi D/L = 6$ are ($\pi D = 0.6 \text{ m}$, $L = 0.1 \text{ m}$) and ($\pi D = 0.3 \text{ m}$, $L = 0.05 \text{ m}$). This indicates that combustion chambers with vastly different geometries might display similar behavior when they have the same aspect ratio. A similar finding has been reported by Tsuboi et al. [8]. Note,

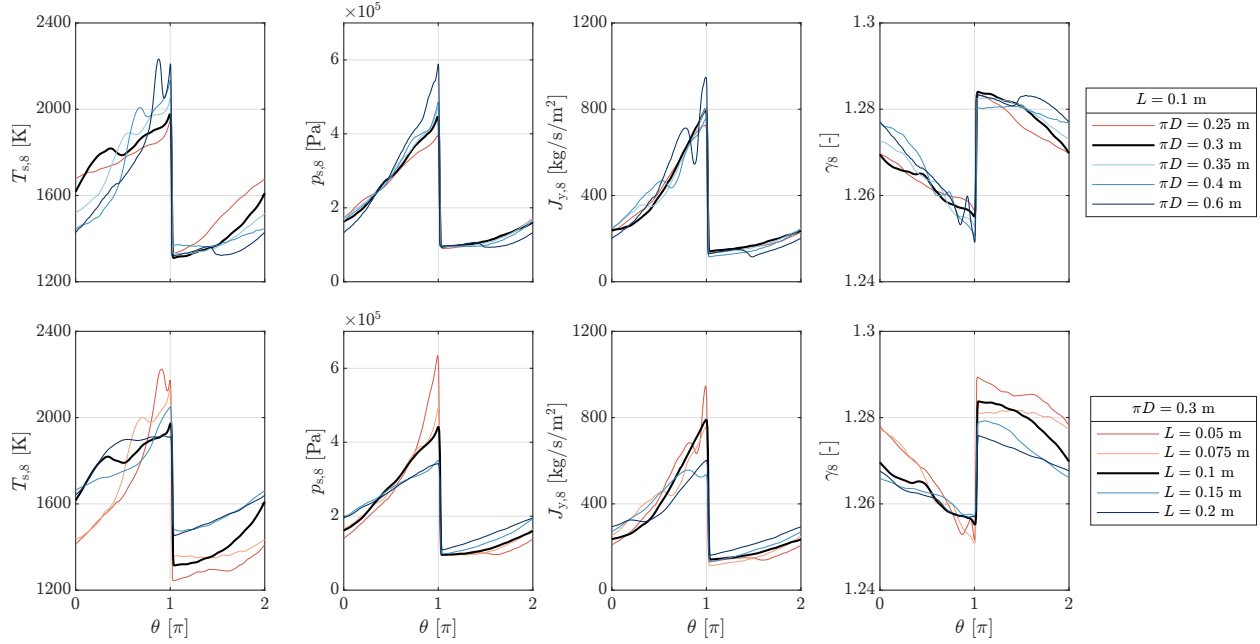


Fig. 2 Unsteady outlet state (station 8) for varying combustor circumference at $L = 0.1$ m (top row) and varying axial length at $\pi D = 0.3$ m (bottom row). The baseline-case is drawn in a thick, black line. Oblique shock is at $\theta = \pi$, travelling from left to right.

that this similarity only exists if cases are compared with respect to the phase angle. The temporal signal of the above rotating shock structure is not equal but changes in frequency approximately inversely proportional with πD .

B. Quantification of Performance

For all cases, the fluctuation in axial mass flux is very high with most of the mass flow contained in the region behind the oblique shock. This also corresponds to the region where the flow is at its highest enthalpy. Consequently, most of the high enthalpy portion of the flow is contained in a relatively small fraction of the flow field. Care must therefore be taken when averaging the outlet state to accurately preserve the information of the flow's overall enthalpy and ability to do work. A non-dimensional performance characteristic is nonetheless desired to allow for easy comparison between cases. Equivalent Available Pressure (EAP) is a frequently used performance criterion for RDC. It was first defined by Kaemming and Paxson [14] as the "flow stagnation pressure which is representative of flow's ability to do work or provide thrust". EAP enables the calculation of Pressure Gain (PG), an intuitive metric that compares PG performance

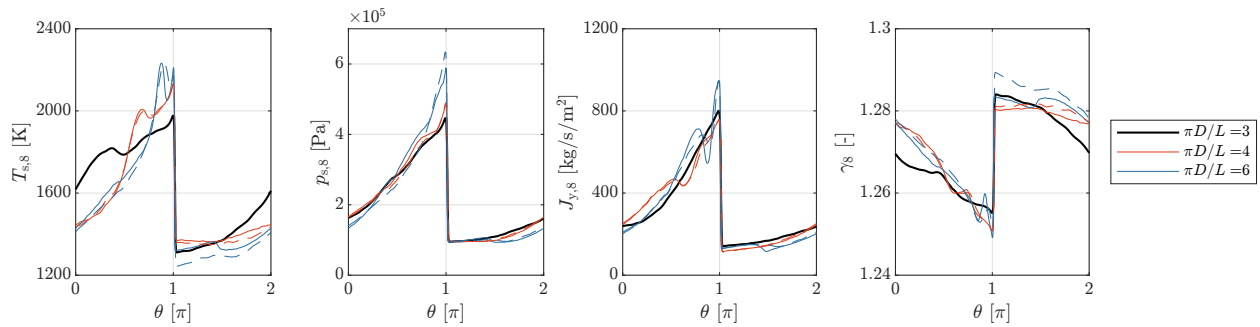


Fig. 3 Unsteady outlet state (station 8) for varying combustor aspect ratio. Two lines are drawn for each aspect ratio. Solid lines mark cases where L is at the baseline value (0.1 m) and πD is varied. Dashed lines mark cases, where πD is at the baseline value (0.3 m) and L is varied.

with that of an isobaric combustion process. The ideal EAP will be referred to as EAP_i in this paper. In the final equation of the suggested EAP_i methodology, γ is used in the exponent:

$$EAP_i = p_0 \left(\frac{\bar{T}_{t,8}}{\tilde{T}_{ei}} \right)^{\frac{\gamma}{\gamma-1}} \quad (2)$$

Where \tilde{T}_{ei} is the ideal exit static temperature. In our case, however, the NASA polynomials are used as caloric equation of state instead of defining constant heat capacities. Consequently, the heat capacities and their ratio vary in space and time. Because EAP_i must be non-dimensional, some kind of averaged γ ($\bar{\gamma}$) must be used instead. Fig. 2 shows that γ fluctuates by a few percent at the outlet plane. One might consider this insignificant and apply an arbitrary average or assume a typical value for this step. It will be shown, however, that significant distortions can occur this way. Closer inspection of Equation 2 reveals a very strong γ -dependency: Consider a temperature ratio $\bar{T}_{t,8}/\tilde{T}_{ei} = 1.5$, $\gamma = 1.25$ and $p_0 = 1$ bar. Eq. 2 yields an EAP_i of 7.59 bar. If $\gamma = 1.24$ is chosen instead, EAP_i becomes 8.12 bar, corresponding to an increase of almost 7%. We can conclude that obtaining an appropriate average for γ is very important because small changes due to averaging can have a disproportional effect on EAP_i . To bypass this issue, a different approach to quantify performance is taken in this paper. Similarly to EAP_i , we want the performance indicator to reflect the flow's ability to do work. The desired methodology, however, should not require $\bar{\gamma}$ and, where γ is used, the sensitivity should be lower. We thus define the Isentropically Available Work (IAW) as "the energy available for conversion to work in an isentropic downstream process". The following method is applied to obtain IAW:

- 1) At the outlet plane, calculate the total enthalpy of each flow segment:

$$h_{t,8} = h_{s,8} + \frac{u_{z,8}^2}{2} + \frac{u_{x,8}^2}{2} \quad (3)$$

- 2) Isentropically expand each flow segment to ambient pressure:

$$T_{s,10} = T_{s,8} \left(\frac{p_{s,10}}{p_{s,8}} \right)^{\frac{\gamma_8-1}{\gamma_8}} \quad (4)$$

This step assumes γ to be constant over the expansion, yet it is still spatially resolved and no average needs to be applied. The inaccuracy of this assumption does not have a drastic effect on the result because eq. 4 has the $\gamma - 1$ term in the numerator of the exponent (in contrast to Eq. 2).

- 3) Calculate the enthalpy difference of the expansion using the caloric equation of state. Δh is the pre-expansion kinetic energy plus the sensible enthalpy available for conversion to kinetic energy or work in an isentropic expansion to ambient pressure.

$$\Delta h = h_{t,8} - h_{s,10} \quad (5)$$

- 4) IAW is the mass flux average of the available kinetic energy:

$$IAW = \overline{\Delta h} = \frac{\sum \Delta h \cdot \rho_8 \cdot u_{z,8}}{\sum \rho_8 \cdot u_{z,8}} \quad (6)$$

- 5) In EAP_i computation, nonaxial kinetic energy is assumed not to be available to do work. Therefore the method is repeated with the nonaxial kinetic energy term being dropped in Equation 3 and the result is denoted as IAW_{ax} .

We would expect EAP_i to represent IAW_{ax} , with any differences resulting from methodology, rather than definition. To enable comparison between both metrics, they are first translated into a common dimension. We chose annulus power density (PD) to do so because it allows for easy comparison of cases with different combustor size. We multiply IAW_{ax} with the annulus mass flux to derive an annulus power density:

$$PD(IAW_{ax}) = IAW_{ax} \cdot J_{3.2} \quad (7)$$

To compute EAP_i , two choices for $\bar{\gamma}$ are tested: an area-average (result denoted as $EAP_{i,\gamma aa}$) and a mass-flux-average (result denoted as $EAP_{i,\gamma mf}$). EAP_i must then be translated to power. First, compute the local power density of each flow segment using the local exhaust velocity:

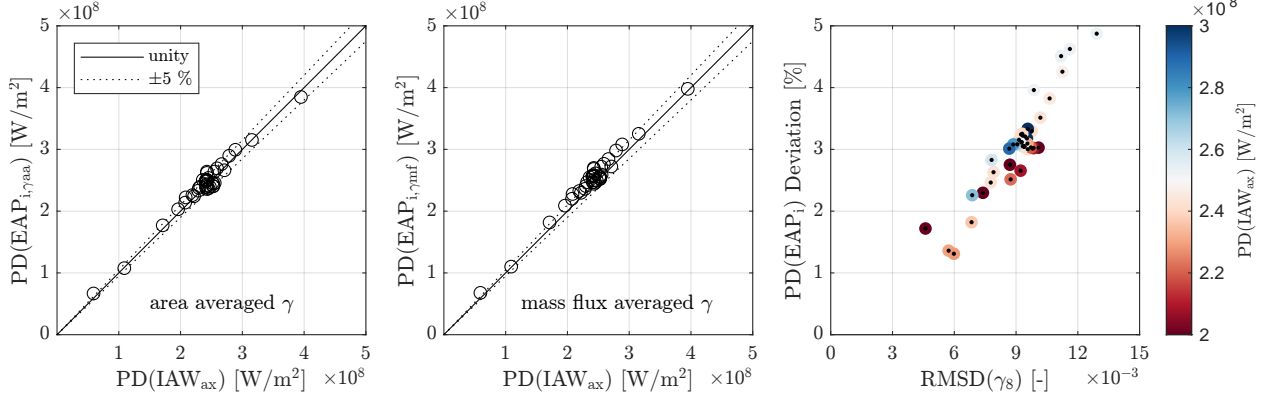


Fig. 4 Correlation between IAW and EAP_i when γ in the final equation of EAP_i calculation is area averaged (left) and when mass flux averaged (middle). The effect of the average is scattered against the RMSD of γ_8 and color-coded by PD(IAW_{ax}) (right).

$$\text{pd}(\text{EAP}_i) = \text{EAP}_i \cdot u_{z,8} \quad (8)$$

Mass flux average the local power density and normalize to annulus area:

$$\text{PD}(\text{EAP}_i) = \frac{\sum \text{pd}(\text{EAP}_i) \cdot \rho_8 \cdot u_{z,8}}{\sum \rho_8 \cdot v_{z,8}} \cdot \frac{A_8}{A_{3.2}} \quad (9)$$

The resulting annulus power densities are compared in Figure 4. When γ is area-averaged, the power densities appear closely correlated with a deviation below 5% for almost all data points (left). When a mass-flux-average is applied instead, PD(EAP_{i,mf}) generally predicts higher values than PD(IAW_{ax}) (middle). Because the deviations are difficult to perceive at this scale, the PD(EAP_i) deviation is computed according to Equation 10.

$$\text{PD}(\text{EAP}_i) \text{ Deviation} = \frac{\text{PD}(\text{EAP}_{i,\gamma_{mf}}) - \text{PD}(\text{EAP}_{i,\gamma_{aa}})}{\text{PD}(\text{IAW}_{\text{ax}})} \quad (10)$$

Deviations between both averages result from fluctuations in γ and their magnitude is expected to depend on the magnitude of the fluctuation. To quantify the magnitude of the γ -fluctuation, the root mean square deviation as defined by Equation 11, where $\bar{\gamma}_8$ is the arithmetic mean (equivalent to area-average for a uniform grid) and n the number of elements, is computed.

$$\text{RMSD}(\gamma_8) = \sqrt{\frac{\sum (\gamma_8 - \bar{\gamma}_8)^2}{n}} \quad (11)$$

Fig. 4 (right) shows the effect of the γ -average scattered against RMSD(γ_8). We observe that both quantities are indeed correlated. Data points are color-coded by PD(IAW_{ax}) to demonstrate that there is no underlying relation with the magnitude of the power density. The mass-flux-average leading to higher EAP_i compared to the area-average is expected, because γ is lowest in the region right behind the oblique shock, where mass-flux is highest. Subsequently, the mass-flux-average is always lower compared to the area-average and thus leads to higher EAP_i. We conclude that the area-average is the conservative choice, when EAP_i methodology is applied in the case of $\gamma \neq \text{const}$. In order to avoid the problems associated with the γ -dependency of Eq. 2 and the need to obtain $\bar{\gamma}$, IAW and IAW_{ax} are used as performance indicators in the following analysis.

C. Performance Dependency on Varied Parameters

The variation of IAW and IAW_{ax} with respect to relative changes in each parameter is depicted in Figure 5. For the baseline case, IAW = 1.01 MJ kg⁻¹ and IAW_{ax} = 0.97 MJ kg⁻¹. The flow's average stagnation enthalpy \bar{h}_t is approximately the same for all cases because the injector plenum temperature (i.e. thermal enthalpy of the injected material) and the fuel-air ratio (i.e. chemical energy available for conversion) remain the same. Small changes in the amount of released heat (and subsequently \bar{h}_t) can still occur as a result of (i) small deviations between the cases nominal

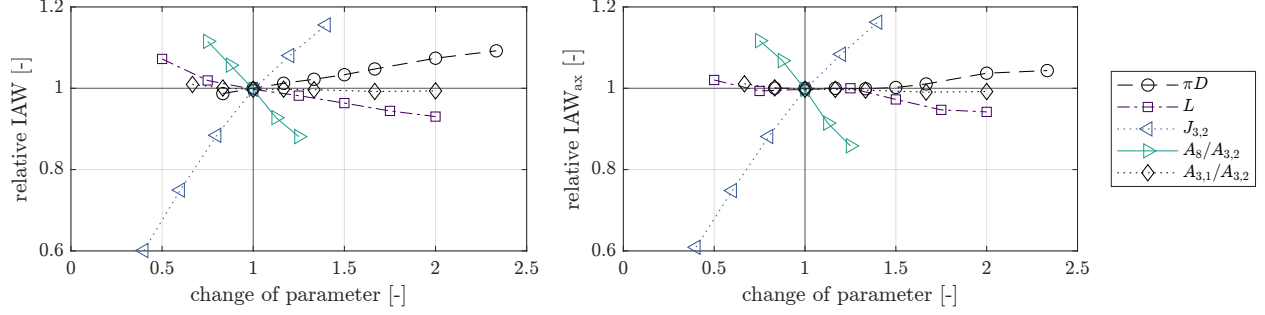


Fig. 5 Sensitivity analysis for IAW and PD(IAW_{ax}). Intersection of black lines marks the baseline case.

equivalence ratio and the actual converged equivalence ratio, and (ii) a different fuel distribution in the refilling zone leading to a different fraction of unburned fuel. For this data-set \bar{h}_t varies by less than 1.5% compared to the base case, where $\bar{h}_t = 2.68 \text{ MJ kg}^{-1}$. Trends seen in Fig. 5 thus reflect the quality (i.e. degree of availability) of the flow's average stagnation enthalpy, rather than its quantity. In other words, the trends result from changes in entropy, rather than energy.

Annulus mass flux $J_{3,2}$ and outlet throat to annulus area ratio $A_8/A_{3,2}$ have the strongest effect on IAW and their influence is approximately linear. This matches with experimental observations in PG measurements by Bach et al. [17]. The contribution of non-axial energy is relatively low, and thus changes in IAW_{ax} are very similar. The effect of combustor circumference πD and axial length L is much smaller than that of $J_{3,2}$ and $A_8/A_{3,2}$, but yet significant. Here, the effect on IAW is significantly higher, than that on IAW_{ax}. Irreversibilities due to processing in the oblique shock are expected to be the driver behind the changes in IAW and IAW_{ax} with respect to πD and L . It should be noted though that increasing the chamber diameter is expected to also increase the number of co-rotating detonation waves in a way that the length of each respective wave (i.e. combustor circumference divided by the number of waves) does not increase by more than 100% [3]. We have therefore reason to expect that the effect of combustor diameter in an actual RDC is even lower than in Fig. 5. The effect of wave number and axial length has previously been studied by Yi et al. [9]. The authors also report a significant increase in total pressure loss (i.e. flow irreversibility) in cases with more oblique shock processing (increase in either the number of waves or axial length). They do, however, also report a slight increase in thrust and ISP for those cases. Schwer and Kailasanath [10] report no significant effect of diameter or axial length on ISP as long as the flow is fully supersonic. The oblique shock is expected to disproportionately dissipate non-axial energy, which could explain the reduced effect on IAW_{ax} (and possibly ISP) where this energy is considered as non-available anyways.

D. Flow Field Dependency on Varied Parameters

To describe the geometry of the flow field, detonation height H and oblique shock angle α are computed. To obtain H , the circumferential gradient of fuel mole-fraction is first computed. This gradient corresponds to the fuel consumption in the detonation. H is then defined as axial length of the region, where significant fuel consumption takes place. To obtain α , two axial positions $z_1 = H + 5 \Delta x$ and $z_2 = L - 15 \Delta x$ are defined. The reasoning behind those choices is that (i) there should be some clearance between z_1 and the triple point to ensure the shock is fully established, (ii) that the measuring window should be as large as possible to reduce the numerical uncertainty, and (iii) that z_2 should be upstream of the convergent section of the domain in case the shock changes shape in that region. At both z , the circumferential position of the shock x_1 and x_2 , respectively, is obtained by finding the maximum in the circumferential pressure gradient. α is then computed according to Equation 12. This approach assumes the shock to be approximately straight, which is typically the case (see e.g. Figure 7). The circumferential position of the shock can only be known as a multiple of Δx , therefore the numerical uncertainty due to discretization is taken into account. If the oblique shock is orthogonal to the outlet plane, then $\alpha = 90 \text{ deg}$. If it is parallel, then $\alpha = 0$.

$$\alpha_{\pm} = \arctan \left(\frac{z_2 - z_1}{x_2 - x_1 \mp \Delta x} \right) \quad (12)$$

Dividing the detonation height by the combustor axial length yields the dimensionless detonation height H/L , which measures the axial fraction of the combustor taken up by the detonation. Figure 6 shows, that H/L strongly correlates with the oblique shock angle α (left). The effect of individual parameters on the oblique shock angle is broken

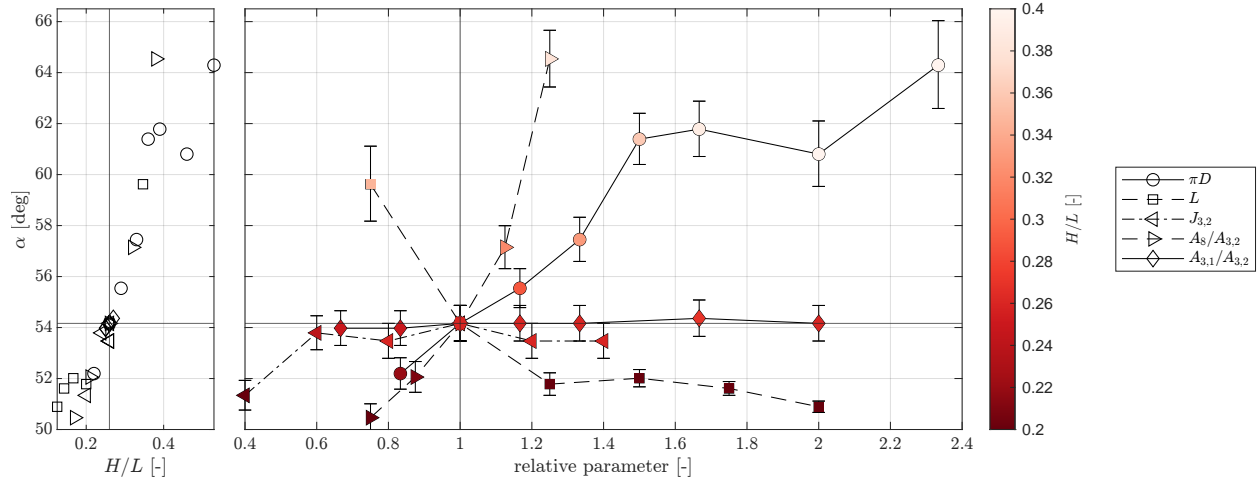


Fig. 6 Correlation between oblique shock angle and H/L (left) and variation in with respect to the studied parameters (right). For $L = 0.05$ m, the distance between the axial measuring points is too low to obtain α reliably and the point is excluded in this figure. Intersection of black lines marks the baseline case.

down in Fig. 6 (right). Here, error-bars indicate the numerical uncertainty in the angle resulting from the discrete grid. We observe that the outlet throat to annulus area ratio has by far the strongest effect on the oblique shock angle, followed by πD . Interestingly, axial length seems to effect α when it is relatively low (below ≈ 1.2 of the base case), but appears to have no effect on α beyond this value. This trend suggests, that α might be independent of the annulus size, when the detonation height is relatively small compared to the axial length (i.e. low H/L). The parameter-space investigated in this paper, however, does not cover the respective range sufficiently to draw a conclusion in that regard. The oblique shock angle is especially important if the integration of downstream components (e.g. guide vanes, turbine) is considered. Experimental research conducted on a RDC equipped with nozzle guide vanes indicates that reflections of the oblique shock impact RDC operation and performance [18]. The apparent independence of α and mass-flux past the choking limit implies that RDCs can be operated over a large range of thermal power without major changes in the shock angle, which is expected to be beneficial for turbine design. Strong variations in α with respect to the outlet throat to annulus area ratio, on the other hand, imply a strong coupling between RDC and downstream components.

There is a second important relation to consider when discussing the oblique shock's effect on performance: The process of shock compression is irreversible and is therefore expected to negatively effect thermal cycle efficiency. Because each streamline experiences a unique thermodynamic cycle, we quantify how much of the mass passes the oblique shock before being ejected from the combustor, or, because streamlines might pass the oblique shock multiple times, how often the mass is processed in the oblique shock, on average. In order to estimate this value, the following mechanism is applied:

- 1) For each cell at the outlet plane: draw a streamline back to the inlet plane, that represents the "history" of the mass contained in that cell. In order to do so, the flow field is assumed to be stationary in its respective relative frame of reference.
- 2) Analyze entropy, stagnation enthalpy (relative frame) and density along each streamline. If a simultaneous discontinuity in both, entropy and density is observed, this is considered to be a shock. If an additional discontinuity in stagnation enthalpy is observed, it is considered to be the detonation itself.
- 3) The number of adiabatic shocks (i.e. excluding the detonation) is counted for each streamline. This number indicates how often the respective parcel of mass has been processed in the oblique shock before reaching the outlet plane.
- 4) This number is then mass flux averaged over all streamlines and the result is referred to as the *shock flow number*.

Figure 7 shows the streamlines drawn from the outlet plane back to the inlet plane. Here, only every 25th streamline is drawn for the purpose of visualization. Black streamlines do not pass through the oblique shock, green ones do. Figure 8 shows that there is a strong correlation between the shock flow number and the dimensionless detonation height H/L . πD , L and $A_8/A_{3,2}$ vary significantly in both quantities and appear to follow the correlation. For the other parameters, neither quantity exhibits significant changes. Interestingly, the correlation can be pretty accurately

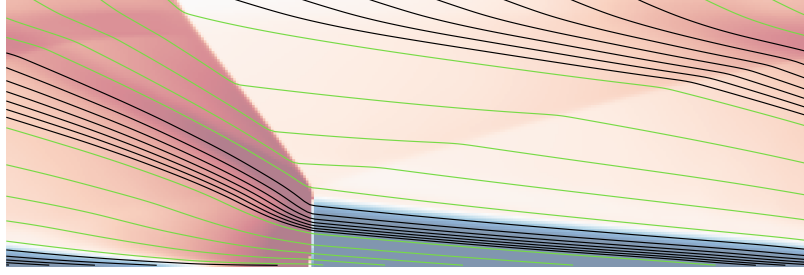


Fig. 7 Visualization of the flow regimes for the baseline case. Streamlines not passing through the oblique shock are drawn in black, streamlines passing through the shock are drawn in green. For the purpose of visualization, only every 25th streamline is drawn in this figure.

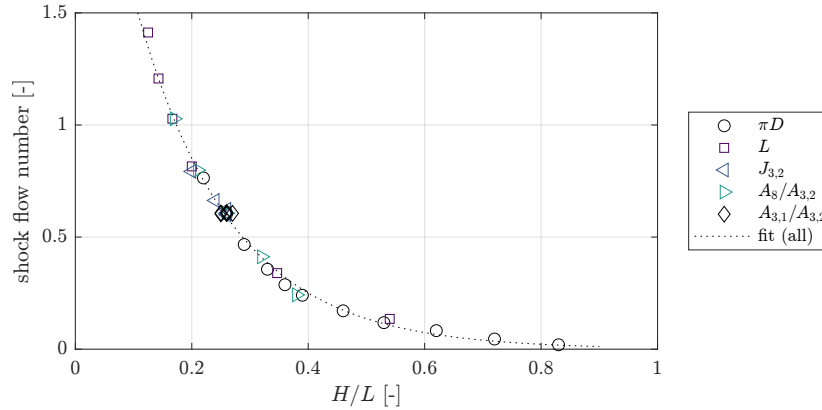


Fig. 8 Correlation between H/L and shock flow number. A fit of the form $y = a \cdot e^{b \cdot x}$ is added.

($R^2 = 0.98$) described using an exponential function of form $y = a \cdot e^{b \cdot x}$ with $a = 2.89$ and $b = -6.41$.

E. Discussion of Loss Mechanisms

The shock flow number is expected to show a negative correlation with IAW because entropy increases with shock processing and thus less of the flows energy remains available for conversion to work. This correlation is depicted in Figure 9. For changes in both circumference and axial length, deviations in IAW and IAW_{ax} can be explained by deviations in the amount of post-detonation shock processing. As expected, IAW_{ax} is less affected by the shock flow number, because the dissipation primarily affects non-axial energy. Consequently, oblique shock processing is not expected to have significant effect on thrust, even if a wide range of combustor (and flow field) geometries are considered. Performance deviations due to varying mass flux and outlet restriction cannot be explained this way: Increasing annulus mass flux past the choking condition at the outlet throat does not yield further changes to the flow field geometry, and thus has no effect on the shock-processing. Performance nevertheless continues to increase with $J_{3,2}$. Restricting the outlet throat yields higher performance while simultaneously increasing the amount of shock processing. In both cases, performance variation cannot be explained by shock processing. Instead, a stronger underlying mechanism must cause the change in performance: When the outlet throat is choked, both an increase in mass flux and a decrease of the throat area is accompanied by an increase of the overall chamber pressure. It is hypothesized that this increase in chamber pressure drives the gain in performance. Furthermore, higher chamber pressure is accompanied by a corresponding increase in the injector supply pressure(s), leading to lower injectant entropy.

IV. Conclusions

In this study, the effect of combustor circumference, axial length, outlet throat area and air injector area on RDC flow field and performance has been investigated. The RDC outlet state is highly fluctuating for all cases with the magnitude of the fluctuation depending on the proximity of the detonation wave and the outlet plane. At cases with equal

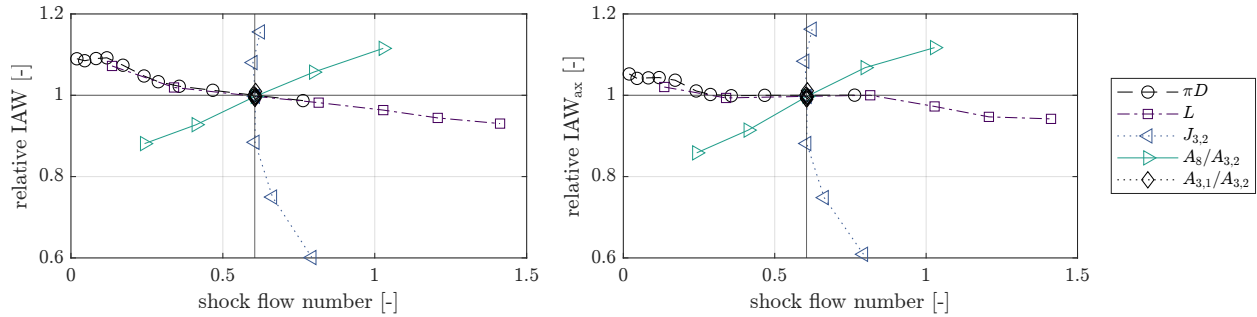


Fig. 9 Correlation between shock flow number and IAW (left) and $I_{AW_{ax}}$ (right).

combustor aspect ratio, the relative proximity between detonation and outlet is similar, and there exists a subsequent similarity in the outlet state. If no constant- γ assumption is made, γ is also subject to significant fluctuations. It has been demonstrated that the generalization of EAP_i-methodology for variable γ is not trivial and can introduce significant distortions if not handled carefully. When EAP_i-methodology is used in the case of $\gamma \neq const.$, area averaging γ is the conservative approach compared to mass-flux averaging. An alternative method to quantify performance, Isentropically Available Work, is applied to avoid this issue. IAW closely matches EAP_i, when γ is area averaged. Annulus mass flux and outlet throat area show by far the strongest effect on IAW, but variations in circumference and axial length still have a significant effect. This effect is reduced, however, when non-axial energy is excluded (i.e. propulsive applications). For all cases studied in this work, deviations in performance result from deviations in entropy because the average stagnation enthalpy is held approximately constant. The oblique shock angle varies in the range of approximately 50 deg to 65 deg and is correlated to the specific detonation height. Of the individual parameters, outlet throat area has the strongest effect on the oblique shock angle, followed by diameter. In order to quantify the amount of adiabatic shock processing the flow experiences, the shock flow number is introduced. Our results suggest that there exists an approximately exponential relationship between the shock flow number and the specific detonation height. The nature of this correlation is subject to extension of this study. Performance effects of combustor diameter and axial length correlate with variations in the shock flow number, indicating that irreversibilities associated with the oblique shock are indeed the driving mechanism. For variation in mass flux and outlet restriction, an increase of pressure in the air injector plenum and the refilling zone is expected to lead to decreased entropy generation.

Diameter and axial length have received limited attention in RDC performance characterization, partly because their effect on propulsive performance appears very low. It has been shown in this study, however, that the work available for downstream processes can be significantly affected. This study provides an estimation of the oblique shock irreversibilities to be expected for a given geometry and relates the effect to geometric properties of the flow field. Future research will be directed towards the effect of back pressure, reflected shock waves from downstream geometry and acoustic resonance introduced by a non-uniform outlet.

Acknowledgments



This project has received funding from the European Union's Horizon 2020 research and innovation programme under the Marie Skłodowska-Curie grant agreement No 956803.

The authors gratefully acknowledge support by the German Research Foundation (DFG) as part of the research grant 317741329.

References

- [1] Stathopoulos, P., "Comprehensive Thermodynamic Analysis of the Humphrey Cycle for Gas Turbines with Pressure Gain Combustion," *Energies*, Vol. 11, No. 12, 2018, p. 3521. <https://doi.org/10.3390/en11123521>, URL <http://www.mdpi.com/1996-1073/11/12/3521>.
- [2] Bach, E., Stathopoulos, P., Paschereit, C. O., and Bohon, M. D., "Performance analysis of a rotating detonation combustor based on stagnation pressure measurements," *Combustion and Flame*, Vol. 217, 2020, pp. 21–36. <https://doi.org/10.1016/j.combustflame.2020.03.017>, URL <https://linkinghub.elsevier.com/retrieve/pii/S0010218020301188>.

- [3] Bykovskii, F. A., Zhdan, S. A., and Vedernikov, E. F., “Continuous Spin Detonations,” *Journal of Propulsion and Power*, Vol. 22, No. 6, 2006, pp. 1204–1216. <https://doi.org/10.2514/1.17656>, URL <https://arc.aiaa.org/doi/10.2514/1.17656>.
- [4] Tellefsen, J., King, P., Schauer, F., and Hoke, J., “Analysis of an RDE with Convergent Nozzle in Preparation for Turbine Integration,” *50th AIAA Aerospace Sciences Meeting including the New Horizons Forum and Aerospace Exposition*, American Institute of Aeronautics and Astronautics, Nashville, Tennessee, 2012. <https://doi.org/10.2514/6.2012-773>, URL <https://arc.aiaa.org/doi/10.2514/6.2012-773>.
- [5] Brophy, C. M., and Codoni, J., “Experimental Performance Characterization of an RDE Using Equivalent Available Pressure,” *AIAA Propulsion and Energy 2019 Forum*, American Institute of Aeronautics and Astronautics, Indianapolis, IN, 2019. <https://doi.org/10.2514/6.2019-4212>, URL <https://arc.aiaa.org/doi/10.2514/6.2019-4212>.
- [6] Schwer, D., and Kailasanath, K., “Numerical investigation of the physics of rotating-detonation-engines,” *Proceedings of the Combustion Institute*, Vol. 33, No. 2, 2011, pp. 2195–2202. <https://doi.org/10.1016/j.proci.2010.07.050>, URL <https://linkinghub.elsevier.com/retrieve/pii/S1540748910003159>.
- [7] Sousa, J., Paniagua, G., and Collado Morata, E., “Thermodynamic analysis of a gas turbine engine with a rotating detonation combustor,” *Applied Energy*, Vol. 195, 2017, pp. 247–256. <https://doi.org/10.1016/j.apenergy.2017.03.045>, URL <https://linkinghub.elsevier.com/retrieve/pii/S0306261917302684>.
- [8] Tsuboi, N., Watanabe, Y., Kojima, T., and Hayashi, A. K., “Numerical estimation of the thrust performance on a rotating detonation engine for a hydrogen–oxygen mixture,” *Proceedings of the Combustion Institute*, Vol. 35, No. 2, 2015, pp. 2005–2013. <https://doi.org/10.1016/j.proci.2014.09.010>, URL <https://linkinghub.elsevier.com/retrieve/pii/S1540748914004313>.
- [9] Yi, T.-H., Lou, J., Turangan, C., Choi, J.-Y., and Wolanski, P., “Propulsive Performance of a Continuously Rotating Detonation Engine,” *Journal of Propulsion and Power*, Vol. 27, No. 1, 2011, pp. 171–181. <https://doi.org/10.2514/1.46686>, URL <https://arc.aiaa.org/doi/10.2514/1.46686>.
- [10] Schwer, D., and Kailasanath, K., “Numerical Study of the Effects of Engine Size on Rotating Detonation Engines,” *49th AIAA Aerospace Sciences Meeting including the New Horizons Forum and Aerospace Exposition*, American Institute of Aeronautics and Astronautics, Orlando, Florida, 2011. <https://doi.org/10.2514/6.2011-581>, URL <https://arc.aiaa.org/doi/10.2514/6.2011-581>.
- [11] Klopsch, R., Garan, N., Bohon, M., Bach, E., Asli, M., and Stathopoulos, P., “2D Euler Modeling of Rotating Detonation Combustion in Preparation for Turbomachinery Matching,” *AIAA SCITECH 2022 Forum*, American Institute of Aeronautics and Astronautics, San Diego, CA & Virtual, 2022. <https://doi.org/10.2514/6.2022-0836>, URL <https://arc.aiaa.org/doi/10.2514/6.2022-0836>.
- [12] Burke, M. P., Chaos, M., Ju, Y., Dryer, F. L., and Klippenstein, S. J., “Comprehensive H₂/O₂ kinetic model for high-pressure combustion: Comprehensive H₂/O₂ Kinetic Model for High-Pressure Combustion,” *International Journal of Chemical Kinetics*, Vol. 44, No. 7, 2012, pp. 444–474. <https://doi.org/10.1002/kin.20603>, URL <https://onlinelibrary.wiley.com/doi/10.1002/kin.20603>.
- [13] Goodwin, David G, Speth, Raymond L, Moffat, Harry K, and Weber, Bryan W, “Cantera: An Object-oriented Software Toolkit for Chemical Kinetics, Thermodynamics, and Transport Processes,” , Feb. 2021. <https://doi.org/10.5281/ZENODO.4527812>, URL <https://zenodo.org/record/4527812>.
- [14] Kaemming, T. A., and Paxson, D. E., “Determining the Pressure Gain of Pressure Gain Combustion,” *2018 Joint Propulsion Conference*, American Institute of Aeronautics and Astronautics, Cincinnati, Ohio, 2018. <https://doi.org/10.2514/6.2018-4567>, URL <https://arc.aiaa.org/doi/10.2514/6.2018-4567>.
- [15] Walters, I. V., Journell, C., Lemcherfi, A. I., Gejji, R., Heister, S. D., and Slabaugh, C. D., “Performance Characterization of a Natural Gas-Air Rotating Detonation Engine at Elevated Pressure,” *AIAA Propulsion and Energy 2019 Forum*, American Institute of Aeronautics and Astronautics, Indianapolis, IN, 2019. <https://doi.org/10.2514/6.2019-4214>, URL <https://arc.aiaa.org/doi/10.2514/6.2019-4214>.
- [16] California Institute of Technology, “Shock and Detonation Toolbox,” <https://shepherd.caltech.edu/EDL/PublicResources/sdt/>, 2020.
- [17] Bach, E., Paschereit, C., Stathopoulos, P., and Bohon, M. D., “An empirical model for stagnation pressure gain in rotating detonation combustors,” *Proceedings of the Combustion Institute*, Vol. 38, No. 3, 2021, pp. 3807–3814. <https://doi.org/10.1016/j.proci.2020.07.071>, URL <https://linkinghub.elsevier.com/retrieve/pii/S1540748920305216>.
- [18] Bach, E., Paschereit, C. O., Stathopoulos, P., and Bohon, M. D., “Rotating Detonation Wave Direction and the Influence of Nozzle Guide Vane Inclination,” *AIAA Journal*, Vol. 59, No. 12, 2021, pp. 5276–5287. <https://doi.org/10.2514/1.J060594>, URL <https://arc.aiaa.org/doi/10.2514/1.J060594>.